Modeling and Design of the Magnetic Integration of Single- and Multi-Stage EMI Filters

Yitao Liu, *Member, IEEE*, Shiqi Jiang, Weihua Liang, Huaizhi Wang, *Member, IEEE*,
and Jianchun Peng, *Senior Member, IEEE*

***Abstract*—A magnetic integration method of single- and multi-stage electromagnetic interference (EMI) filters is presented. Common-mode and differential-mode inductors are integrated into a single magnetic core unit to significantly reduce the filter volume. A 500-W silicon carbon (SiC) single-phase inverter is used as an experimental platform. The magnetic integration model is designed, and the magnetic circuit analysis is conducted in a simulation to ensure that the core will not reach magnetic saturation under full-load conditions. The feasibility of the proposed method is verified by an EMI test in a simulation and an experiment. Compared with a traditional discrete passive EMI filter, the proposed integrated EMI filters can reduce 40% of the total volume and 69% of the inductor volume in an integrated single-stage EMI filter with satisfactory EMI suppression ability. Although the weight of integrated inductor of integrated multi-stage EMI filter (IMSEF) has 23.8% increment, the IMSEF shows a better EMI suppression ability and 4.6% inductor volume reduction.**

***Index Terms*—Conducted electromagnetic interference (EMI), EMI filter, magnetic integration, multi-stage, single-stage.**

I. Introduction

THE PULSEWIDTH modulation (PWM) method is widely used in power converters. As a typical application, grid-connected inverters benefit from the elimination of lower order current harmonics and the high efficiency with the PWM technique. However, it also increases the level of electromagnetic interference (EMI), especially in higher switching frequency applications [1]–[4]. In recent years, the issue has been particularly prominent with the prevalence of wide-bandgap (WBG) materials, such as silicon carbon (SiC) and gallium nitride (GaN). EMI noise not only affects the normal operation of the equipment itself but also interferes with the surrounding equipment by coupling to the same power grid. For grid-connected systems, EMI noise can pollute the power grid and spread to other electrical equipment, causing severe consequences. Thus, standards such as the International Special Committee on Radio Interference (CISPR) [5] specify the limit of EMI noise that a power converter is allowed to generate. Many solutions have been proposed to make grid-connected systems meet the standard in [6]–[8]. The design of a passive EMI filter (PEF) and magnetic core saturation analysis were introduced in detail in [6]. In [7] and [8], the proposed active EMI filter (AEF) was mainly designed to improve the low-frequency performance of a PEF. The PEF is currently the most widely used method due to the poor stability or undesirable overall effects of the AEF [7], [9]. However, a traditional discrete EMI filter will significantly increase the volume of the converter, although the volume of the harmonic filter can be significantly reduced by the higher switching frequency. Thus, some integration methods have been proposed to reduce the volume of passive EMI filters with higher power density. Two typical solutions are integrated passive filters with a planar printed circuit board (PCB) and integrated inductors with a single core unit [10]–[14]. In [10], a flexible multilayer foil was applied to integrate the filter capacitor with an inductor; however, the presented analysis of the integration method of the inductors was not completed. A novel magnetic integration method with double ring cores was proposed in [11]. This method can indeed reduce the volume to a large extent, while the number of turns of the differential-mode (DM) inductor is related to that of the common-mode (CM) inductor, but the designs are not independent. Previous PEF integration technology has been designed for a single-stage EMI filter. For the case where the initial EMI noise is quite serious, a single-stage EMI filter must be designed with large inductors, which naturally leads to higher parasitic parameters. This can reduce the suppression degree of the high-frequency noise. On the other hand, the magnetic core is more easily saturated under conditions with larger inductance and these factors can be considered for further improvements. A planar inductor used for EMI filter integration was designed, analyzed, and improved in [13]–[15]. Some contributions have been made, but further progress has been limited by the equivalent parallel capacitance of the planar inductors, which is restricted by the dimension, size, and physical structure [14].

This paper presents a systematic method to integrate single- and multi-stage PEFs with EE-type and EIE-type cores that the center leg is twice the width of the outer leg, respectively; it provides volume reduction with enhanced EMI attenuation ability compared with the traditional discrete passive EMI filter (DPEF). The integrated single-stage EMI filter (ISSEF) and integrated multi-stage EMI filter (IMSEF) are modeled, analyzed,

---

Manuscript received December 2, 2018; revised March 3, 2019; accepted April 26, 2019. Date of publication May 8, 2019; date of current version October 18, 2019. This work was supported in part by the Natural Science Foundation of Guangdong Province under Grant 2017A030310317 and in part by the Foundation of Shenzhen Science and Technology Committee under Grant JCYJ20170817100322198. Recommended for publication by Associate Editor F. Costa. *(Corresponding author: Huaizhi Wang.)*

The authors are with the College of Mechatronics and Control Engineering, Shenzhen University, Shenzhen 518060, China (e-mail: liuyt@ieee.org; jiangshiqi2017@email.szu.edu.cn; weihualiang@163.com; wanghz@szu.edu.cn; jcpeng@szu.edu.cn).

Color versions of one or more of the figures in this paper are available online at http://ieeexplore.ieee.org.

Digital Object Identifier 10.1109/TPEL.2019.2915804

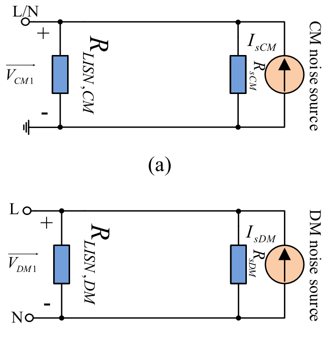

(a)

(b)

Fig. 1. Typical EMI model in the power converter. (a) CM model without EMI filter. (b) DM model without EMI filter.

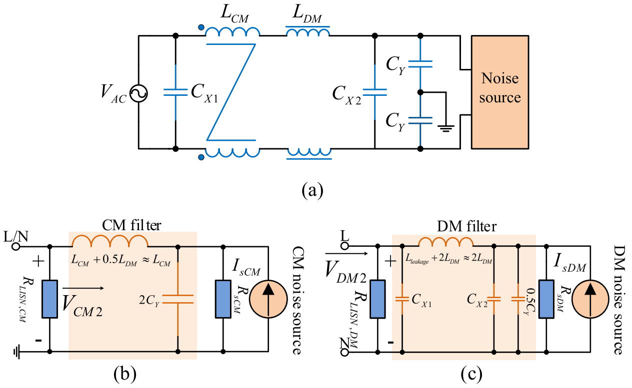

(a)

(b)

(c)

Fig. 2. Typical single-stage EMI filter in the power converter. (a) Integral topology. (b) Equivalent CM model with single-stage EMI filter. (c) Equivalent DM model with single-stage EMI filter.

and designed for application in a silicon carbon single-phase inverter. The feasibility of this design scheme is verified by simulation and experiment. In Section II, the parameter design method of the PEF is introduced briefly. Then, the design and analysis of the proposed ISSEF and IMSEF models are presented in detail in Section III. Finally, the simulation and experimental verifications of the proposed magnetic integration methods as well as the discussion of the experiment results are given in Sections IV and V, respectively. The conclusion is presented in Section VI.

II. PARAMETER DESIGN PROCEDURE OF PEF

The design of the PEF parameters is the basis of the magnetic integration method. In this paper, the detailed theoretical derivation and calculation of the filtering component design of PEF are conducted first. Both the single-stage and multi-stage passive EMI filter for EMI reduction are modeled and analyzed in detail.

A. Analysis and Design of the Single-Stage EMI Filter

Fig. 1(a) and (b) shows the CM and DM model without EMI filter, respectively. The $\overrightarrow{V_{CM1}}$ (or $\overrightarrow{V_{DM1}}$) is the original CM (or DM) noise voltage measure by the line impedance stabilization network (LISN). A typical single-stage EMI filter with an LISN and its equivalent CM and DM models are shown in Fig. 2(a)–(c), respectively, where R_{sCM} and R_{sDM} are the equivalent impedances of the CM noise and DM noise source, respectively, which are commonly regarded as infinite. $\overrightarrow{V_{CM2}}$ (or $\overrightarrow{V_{DM2}}$) is the corresponding noise voltage measure by LISN with the single-stage PEF.

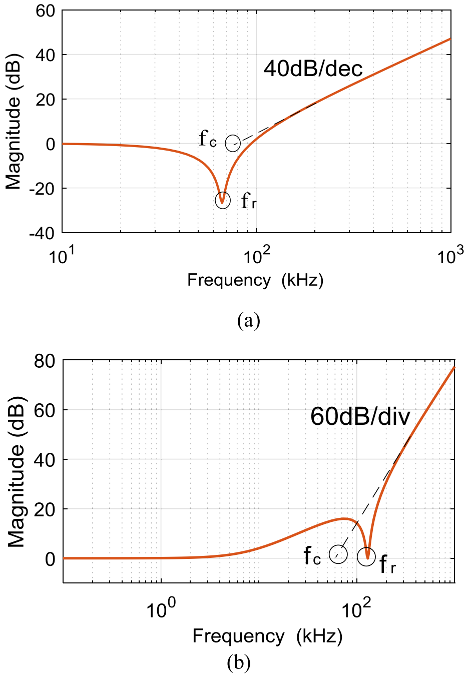

Fig. 3. Insertion loss of a single-stage PEF. (a) CM. (b) DM.

The parameters of the single-stage PEF are designed according to the required insertion losses of the CM and DM modules. The CM and DM insertion losses of a single-stage PEF are derived from (1). Fig. 3 shows the amplitude-frequency curves of the CM and DM insertion losses, which are obtained from (1). The cutoff frequency is designed according to (2), where f_T is the harmonic frequency to be attenuated and V_{req} is the required attenuation at f_T [6]. With the combination of (2) and (3), the parameters of the single-stage PEF can be designed properly

$$\begin{cases} G_{CM}(s) = \dfrac{\overrightarrow{V_{CM1}}(s)}{\overrightarrow{V_{CM2}}(s)} \\ \qquad\quad = 2L_{CM}C_Y s^2 + 2R_{LISN,CM}C_Y s + 1 \\ G_{DM}(s) = \dfrac{\overrightarrow{V_{DM1}}(s)}{\overrightarrow{V_{DM2}}(s)} \\ \qquad\quad = 2L_{DM}C_{X1}C_{X2}R_{LISN,DM}s^3 + 2L_{DM}C_{X2}s^2 \\ \qquad\qquad + R_{LISN,DM}(C_{X1}+C_{X2})s + 1 \end{cases} \tag{1}$$

$$\begin{cases} f_{c-\text{req},CM} = \min\left(f_T \times 10^{-\frac{V_{\text{req}}}{40}}\right) \\ f_{c-\text{req},DM} = \min\left(f_T \times 10^{-\frac{V_{\text{req}}}{60}}\right) \end{cases} \tag{2}$$

$$\begin{cases} f_{c,CM} \approx f_r = \dfrac{1}{2\pi}\sqrt{\dfrac{1}{2L_{CM}C_Y}} \\ f_{c,DM} = \dfrac{1}{2\pi}\sqrt[3]{\dfrac{1}{2L_{DM}C_{X1}C_{X2}R_{LISN,DM}}}. \end{cases} \tag{3}$$

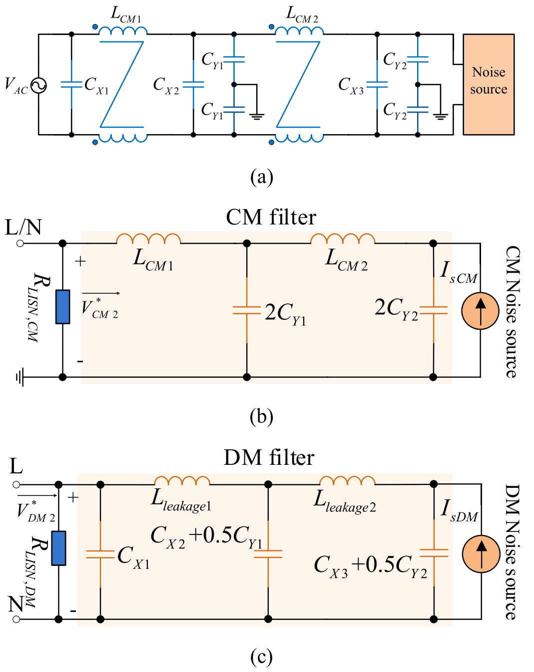

(a)

(b)

(c)

Fig. 4. Typical multi-stage EMI filter. (a) Integral topology. (b) Equivalent CM model. (c) Equivalent DM model.

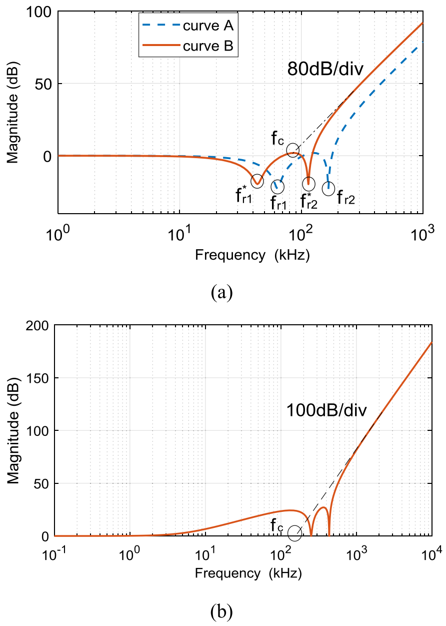

(a)

(b)

Fig. 5. Insertion loss of the multi-stage PEF. (a) CM. (b) DM.

B. Analysis and Design of the Multi-Stage EMI Filter

The topology of the multi-stage PEF is shown in Fig. 4, which can be designed with a smaller inductance due to the better noise suppression performance. In Fig. 4, the CM and DM insertion losses of the multi-stage PEF are derived from (4), and the amplitude-frequency curves of the CM and DM insertion losses are depicted in Fig. 5. The design method of the multi-stage PEF parameters is similar to that of a single-stage PEF

$$\begin{cases} G^*_{CM}(s) = \dfrac{\overrightarrow{V_{CM1}(s)}}{\overrightarrow{V^*_{CM2}(s)}}\ 4L_{CM1}L_{CM2}C_{Y1}C_{Y2}s^4 \\ \quad + 4L_{CM2}C_{Y1}C_{Y2}R_{\text{LISN},CM}s^3 \\ \quad + [2L_{CM2}C_{Y1} + 2L_{CM1}(C_{Y1}+C_{Y2})]s^2 \\ \quad + 2R_{\text{LISN},CM}(C_{Y1}+C_{Y2})s + 1 \\ G^*_{DM}(s) = \dfrac{\overrightarrow{V_{DM1}(s)}}{\overrightarrow{V^*_{DM2}(s)}} \\ \quad = R_{\text{LISN},DM}L_{\text{leakage1}}L_{\text{leakage2}}C_{X1}C_{X2}C_{X3}s^5 \\ \quad + L_{\text{leakage1}}L_{\text{leakage2}}C_{X2}C_{X3}s^4 + R_{\text{LISN},DM} \\ \quad \times [L_{\text{leakage1}}C_{X1}(C_{X2}+C_{X3}) \\ \quad + L_{\text{leakage2}}C_{X3}(C_{X1}+C_{X2})]s^3 \\ \quad + (L_{\text{leakage1}}C_{X2} + L_{\text{leakage1}}C_{X3} \\ \quad + L_{\text{leakage2}}C_{X3})s^2 \\ \quad + R_{\text{LISN},DM}(C_{X1}+C_{X2}+C_{X3})s + 1. \end{cases} \tag{4}$$

The cutoff frequency and its relationship with the elements are determined from (5) and (6). In addition, special attention needs to be paid to the resonance frequency of the CM EMI filter during the design procedure, especially f_{r2}. As shown in Fig. 5(a), curve A is the amplitude–frequency response curve of the equivalent CM filter with initial calculated parameters ($L_{CM} = 0.54$ mH, $C_Y = 2200$ pF), but f_{r2} exceeds 150 kHz in this situation; the EMI noise attenuation will be amplified around this frequency point. Hence, f_{r1} and f_{r2} must be adjusted to be away from the conducted EMI frequency range of 150 kHz–30 MHz. f_{r1} and f_{r2} are determined from (7), which can be used to verify or improve the final designed parameters of the multi-stage PEF. Increasing the C_Y to be 4700 pF and the f_{r2} is successfully decreased below 150 kHz as shown in curve B of Fig. 5(a). On the other hand, the equivalent DM filter is a five-order circuit with a 100 dB/dec attenuation rate on the high-frequency EMI noise, which is shown in Fig. 5(b). Thus, the required DM inductance is quite small, which is commonly replaced by the leakage inductance of the CM inductor

$$\begin{cases} f_{c,CM} = \dfrac{1}{2\pi}\sqrt[4]{\dfrac{1}{4C_{Y1}C_{Y2}L_{CM1}L_{CM2}}} \\ f_{c,DM} = \dfrac{1}{2\pi}\sqrt[5]{\dfrac{1}{R_{\text{LISN},DM}L_{\text{leakage1}}L_{\text{leakage2}}C_{X1}C_{X2}C_{X3}}}. \end{cases} \tag{5}$$

Based on the above analysis of the filtering component design, the design procedure of the ISSEF and IMSEF can be depicted as Fig. 6(a) and (b), respectively. The detailed modeling and analysis of ISSEF and IMSEF are presented in the following

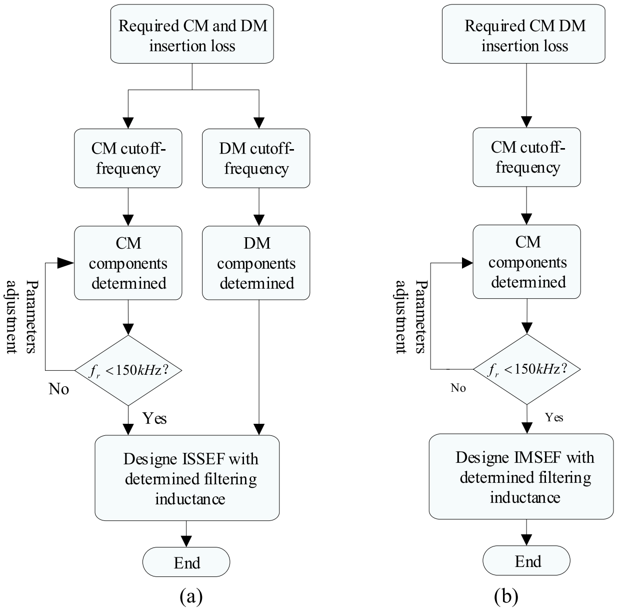

(a) (b)

Fig. 6. Design procedure of integrated inductor. (a) Integrated inductor in ISSEF. (b) Integrated inductor in IMSEF.

section

$$\begin{cases} f_{c-\mathrm{req},CM} = \min\left(f_T \times 10^{-\frac{V_{\mathrm{req}}}{80}}\right) \\ f_{c-\mathrm{req},DM} = \min\left(f_T \times 10^{-\frac{V_{\mathrm{req}}}{100}}\right) \end{cases} \tag{6}$$

$$\begin{cases} f_{r1} = \dfrac{1}{2\pi}\sqrt{\dfrac{3-\sqrt{5}}{2}\dfrac{1}{2L_{CM}C_Y}} \\ f_{r2} = \dfrac{1}{2\pi}\sqrt{\dfrac{3+\sqrt{5}}{2}\dfrac{1}{2L_{CM}C_Y}}. \end{cases} \tag{7}$$

III. DESIGN OF THE ISSEF AND IMSEF

A. Modeling and Analysis of the ISSEF and IMSEF

In this paper, the EE core is used for an ISSEF. The designed structure of the integrated CM and DM inductor is shown in Fig. 7(a). The air gap is designed at the center leg of the core to increase the reluctance; most of the magnetic flux generated on the side leg will flow through the peripheral side legs under CM activation, and therefore, controlling the CM magnetic circuit would simplify the analysis and design. In these structures, N_1 is the winding number of the side legs contributed by each of the L and N lines, N_2 is the winding number of each part of the center leg, and l_g denotes the length of the air gap in the center leg.

The EIE core is applied for an IMSEF. The designed structures of the integrated inductors are shown in Fig. 7(b) and (c). Fig. 7(b) depicts the structure of the EIE magnetic core without an independent DM inductor. The air gaps designed between the E-type and I-type cores can increase the saturated ampere-turns of the core and decouple the upper and lower parts of the magnetic path for simpler analysis and parameter design. In general, the required DM inductance is quite small due to the 100 dB/dec attenuation rate of the multi-stage PEF on the DM noise. It can be replaced by the leakage inductance of the CM inductor, which is approximately 0.1%–2% of the CM choke inductance value [6]. In addition, the winding structure of the magnetic core with an independent DM inductor can be designed as in Fig. 7(c) for a specific situation.

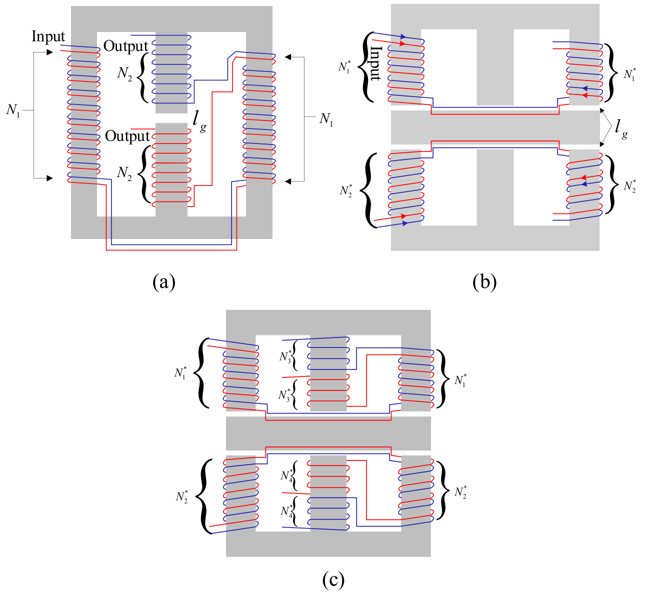

(a) (b)

(c)

Fig. 7. Winding structure of the magnetic core of the ISSEF and IMSEF. (a) EE core in ISSEF. (b) EIE core in IMSEF designed without independent DM inductor. (c) EIE core in IMSEF designed with independent DM inductor.

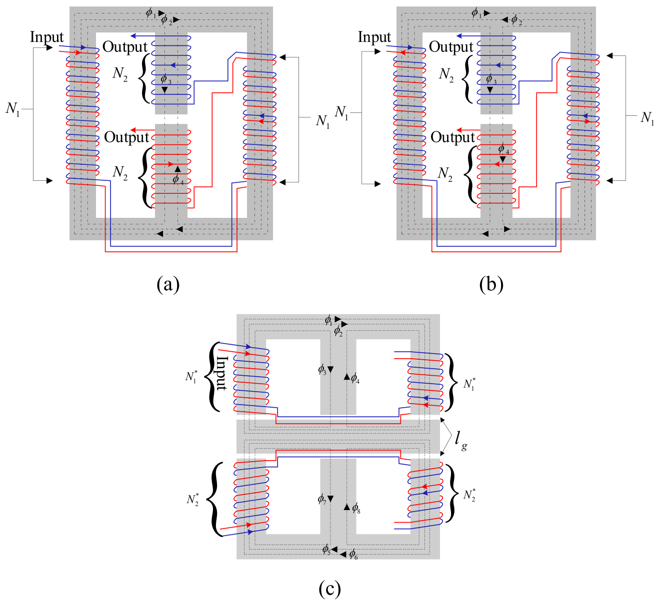

(a) (b)

(c)

Fig. 8. Magnetic coupling of the integrated core under CM and DM activating. (a) EE core in ISSEF under CM activating. (b) EE core in ISSEF under DM activating. (c) EIE core in IMSEF under CM activating.

The magnetic coupling states are shown in Fig. 8(a) and (b) when the integrated magnetic core is applied in the CM and DM noise model of ISSEF. The magnetic flux produced by the windings of the side legs can strengthen each other when the

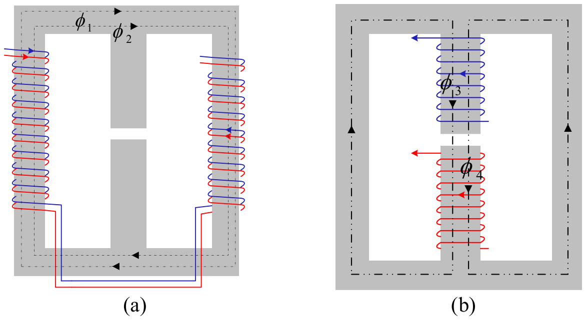

Fig. 9. Simplified magnetic coupling of EE core in ISSEF. (a) CM. (b) DM.

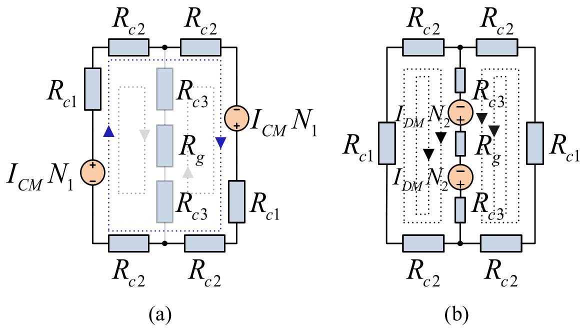

Fig. 10. Equivalent magnetic circuits. (a) Under the CM model. (b) Under the DM model.

CM current flows, while the magnetic flux produced by the two-part windings of the center leg cancel each other. On the other hand, the magnetic flux produced by the windings of the center leg can strengthen each other when the DM current flows, while the magnetic flux produced by the windings of the side legs cancel each other. Fig. 8(c) depicts the magnetic coupling state of EIE core in IMSEF under CM activation. The upper and lower parts act as two CM inductors of IMSEF. The magnetic circuits can be isolated by providing an air gap between the E-type and the I-type magnetic core to achieve the EI-EI effect, which can simplify the magnetic circuit model. The simplified CM and DM magnetic coupling structures of ISSEF are shown in Fig. 9. For the CM model, the reluctance of the center leg is much higher than that of the side legs; thus, the magnetic flux crossing through the center leg can be ignored under CM activation.

B. Magnetic Circuit Modeling and Inductance Calculation of ISSEF and IMSEF

The equivalent CM and DM magnetic circuits of the integrated inductor in ISSEF are shown in Fig. 10, where R_g denotes the air-gap magnetic reluctance of the center leg. R_{c1} and R_{c3} represent the magnetic reluctances of the side leg and center leg, respectively. R_{c2} stands for the magnetic reluctance of the yoke. According to the magnetic circuits above, the self-reluctance and mutual reluctance are equal for the two-part magnetic potential of the CM and DM. $R_{M,CM}$ and $R_{M,DM}$ represent the self-reluctance (or mutual reluctance) for CM and DM, respectively, which are determined from (8) and (9). $R_{\phi 1}$ (or $R_{\phi 2}$) and $R_{\phi 3}$ (or $R_{\phi 4}$) are defined in (10). μ_0 denotes the permeability of air and μ_r stands for the relative permeability of the magnetic core.

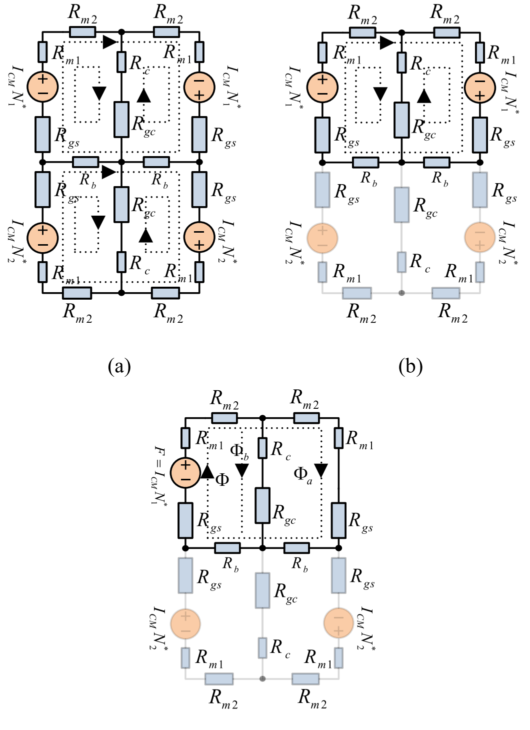

(a)

(b)

(c)

Fig. 11. Magnetic circuit of the IMSEF. (a) Equivalent magnetic circuit. (b) Simplified magnetic circuit. (c) Simplified magnetic circuit for R_M analysis.

$l_{\phi 1}$ and l_c represent the magnetic path lengths of ϕ_1, as shown in Fig. 8(a) [or (b)], and the center leg, respectively. A_s and A_c denote the cross-sectional areas of the side leg and center leg, respectively

$$R_{M,CM} = 2R_{c1} + 4R_{c2} = R_{\Phi 1} \text{ (or } R_{\Phi 2}) \tag{8}$$

$$R_{M,DM} = 0.5R_{c1} + R_{c2} + 2R_{c3} + R_g \approx R_{\Phi 3} \text{ (or } R_{\Phi 4}) \tag{9}$$

$$\begin{cases} R_{\Phi 1} = \dfrac{l_{\Phi 1}}{\mu_r \mu_0 A_s} \\ R_{\Phi 3} = \dfrac{0.5 l_{\Phi 1}}{\mu_r \mu_0 A_s} + \dfrac{l_c - l_g}{\mu_r \mu_0 A_c} + \dfrac{l_g}{\mu_0 A_c}. \end{cases} \tag{10}$$

The contributed CM and DM inductances of the ISSEF can be derived from (11) and (12); accordingly, the parameters of the ISSEF can be appropriately designed

$$L_{CM} = \frac{(2N_1)^2 \mu_0 \mu_r A_s}{l_{\Phi 1}} \tag{11}$$

$$L_{DM} = \frac{(2N_2)^2 \mu_r \mu_0 A_s A_c}{0.5 l_{\Phi 1} A_c + (l_c - l_g) A_s + l_g A_s \mu_r} \times \frac{1}{2}. \tag{12}$$

The magnetic circuit and its simplified model of IMSEF are shown in Fig. 11(a) and (b). R_{m1}, R_{m2}, and R_c denote the magnetic reluctances of the side leg, yoke, and center leg, respectively. R_b represents the reluctance of the I-type core. R_{gs} and R_{gc} represent the air gap reluctances of the side leg and center leg, respectively.

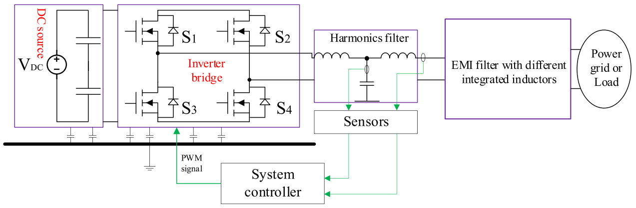

Fig. 12. Single-phase inverter system with EMI filter.

According to the simplified magnetic circuit, the self-reluctance (R_m) can be directly estimated. The mutual reluctance (R_M) stands for the reluctance of magnetic coupling path between the winding groups on the left- and right-side legs. In such a symmetric magnetic circuit, R_M is equivalent to the reluctance from the left-side winding group to the right-side winding group. Thus, the magnetic circuit can be further simplified as shown in Fig. 11(c) for R_M determination, where F and ϕ denote the magnetic potential and total flux produced by the winding group on the left side-leg, respectively. ϕ_a and ϕ_b stand for the right side-leg and center-leg flux produced by the magnetic potential (F), respectively. ϕ_a is indeed the coupled flux, and thus, $R_M = \frac{F}{\phi_a}$. R_m and R_M can be derived from (13) [16]–[18], where R_1 and R_2 are expressed as (14). The magnetic reluctances of all parts are shown in (15), where l_{s1} and l_{s2} denote the lengths of the side leg and yoke, respectively.

The equivalent CM inductor consists of two parts—self-inductance and mutual inductance (*M*), which can be derived from (16). K_M is the coupling coefficient of the inductors produced by the side legs and is given in (17)

$$\begin{cases} R_m = R_1 + R_1//R_2 = R_1 + \dfrac{R_1 R_2}{R_1 + R_2} \\ R_M = \dfrac{F}{\Phi_a} = \dfrac{F}{\Phi \cdot \frac{R_2}{R_1+R_2}} = \dfrac{F}{\Phi} \cdot \dfrac{R_1 + R_2}{R_2} \\ \quad\;\; = R_m \cdot \dfrac{R_1 + R_2}{R_2} = \dfrac{R_1(R_1 + 2R_2)}{R_2} \end{cases} \tag{13}$$

$$\begin{cases} R_1 = R_{m1} + R_{m2} + R_b + R_{gs} \\ R_2 = R_c + R_{gc} \end{cases} \tag{14}$$

$$\begin{cases} R_{m1} = \dfrac{l_{s1}}{\mu_r \mu_0 A_{s1}}, R_{m2} = \dfrac{l_{s2}}{\mu_r \mu_0 A_{s2}} \\ R_c = \frac{l_c}{\mu_r \mu_0 A_c} R_{gc} = \dfrac{l_g}{\mu_0 A_c}, \quad R_{gs} = \dfrac{l_g}{\mu_0 A_s} \end{cases} \tag{15}$$

$$L^*_{CM} = \frac{2N_1^{*2}}{R_m} + 2M = (2 + 2K_M)\frac{N_1^{*2}}{R_m} \tag{16}$$

$$K_M = \frac{R_m}{R_M} = \frac{R_2}{R_1 + R_2}. \tag{17}$$

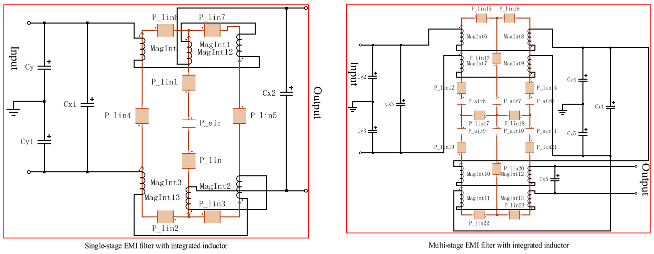

(a) (b)

Fig. 13. Structure of the integrated inductor in the simulation. (a) ISSEF. (b) IMSEF.

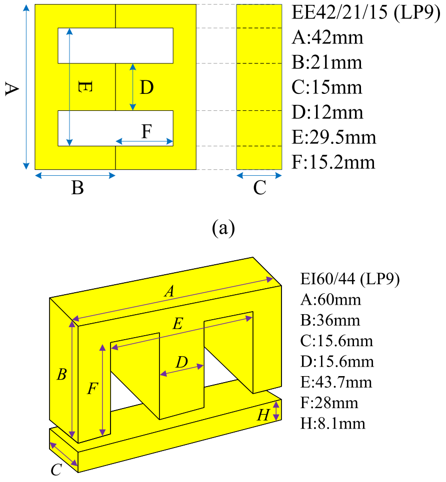

(a)

(b)

Fig. 14. Sizes of the selected magnetic cores. (a) ISSEF. (b) IMSEF.

TABLE I
CHARACTERISTICS OF THE MAGNETIC MATERIAL-LP9

Initial permeability (μ_i)	Power loss (kW/m^3)(100kHz, 200 mT)	Saturation flux density (B_s /mT)	Curie temperature (T_c/°C)
3300±25%	350 (25°C) 300 (80°C) 320 (100°C)	520 (25°C) 410 (100°C)	≥ 215°C

IV. SIMULATION VERIFICATION

In this section, a 500-W single-phase voltage source inverter (VSI), as shown in Fig. 12, is applied in PLECS software for simulation verification. The dc-link voltage is 200 V, the output voltage is ac 110 V/50 Hz, and the switching frequency is 50 kHz. The EMI suppression ability with the ISSEF or IMSEF is verified with the EMI standard EN55011 [19], which defines the measurement frequency from 150 kHz to 30 MHz. The detailed structure of the integrated inductor in the simulation is shown in Fig. 13 [20].

The magnetic cores are selected according to [21] and [22], and the cores selected for the ISSEF and IMSEF are EE42/21/15 (LP9) and EI60/44 (LP9), respectively [23]. The sizes of the cores are shown in Fig. 14. The characteristics of the ferrite magnetic material-LP9 are shown in Table I. In order to meet the previously established integrated inductor simplified models in ISSEF and IMSEF, the branch reluctance with the added air gap must be designed much larger than the reluctance of other magnetic circuit branches. For the magnetic circuit of ISSEF, it is necessary to make the resistance of the center-leg much larger

TABLE II
PARAMETER DESIGN OF THE ISSEF AND IMSEF

Parameters	ISSEF	IMSEF
C_X (μF)	0.1	1
C_Y (pF)	2200	4700
L_{CM} (mH)	1.3	0.54
L_{DM} (μH)	26	0.548
N_1	17	-
N_2	14	-
N_1^* (or N_2^*)	-	19
l_g (mm)	0.9	0.3
Winding diameter (mm)	0.8	0.8

than the resistance of the side-leg, ensuring that the magnetic coupling coefficient between the left- and right-side leg winding groups approximately equals one.

For the magnetic circuit of IMSEF, the branch reluctance with the added air gap must be designed much larger than half of the reluctance of the I-type core. Thus, the condition in (18) should be satisfied, and the appropriate design range of the air gap length can be obtained. Regarding the reluctance of the branch where the air gap is located, it showed ten times the reluctance of other branches as the demarcation point. According to the permeability listed in Table I and the core size shown in Fig. 14, the air-gap length can be calculated as $l_g > 0.244$ mm in ISSEF, $l_{gs} > 0.087$ mm in IMSEF, and $l_{gc} > 0.173$ mm in IMSEF, where l_{gs} and l_{gc} denote the air-gap length of the side leg and center leg in IMSEF, respectively

$$\begin{cases} R_g + 2R_{c3} >> R_{c1} + 2R_{c2} \Rightarrow R_g >> R_{c1} \\ R_{gs} + R_{m1} + R_{m2} >> R_b, R_{gc} + R_c >> R_b. \end{cases} \quad (18)$$

Based on the previous analysis and calculation, the air gap is selected as $l_g =$ 0.9 mm in ISSEF and $l_{gs} = l_{gc} =$ 0.3 mm in IMSEF. With the determination of expected designed values according to the proposed analysis in Section II, the turn number of the windings can be determined according to (11), (12), and (16) with the required filtering inductance. The designed parameters of the ISSEF and IMSEF are listed in Table II. The parameters of the two parts of the IMSEF are designed with the same value, where $C_{Y1} = C_{Y2}$ and $C_{X1} = C_{X2} = C_{X3}$.

Fig. 15(a)–(c) shows the simulated flux distribution of the integrated inductors of the ISSEF and IMSEF under a full load (500 W), $i_g = 4.5$ A. For ensuring that the core will not saturate, the excitation current is set to 4.5 A/50 Hz for CM and DM conditions, the core permeability is set to 3300 according to the datasheet, and the designed model characteristics are consistent with the parameters depicted in Table II. According to the saturation curve of the ferrite core shown in Fig. 15(d), the maximum flux in the core of the integrated inductor of the ISSEF under CM is in the range of 0.43–0.74 of the saturation flux at a temperature of 25–120 °C. The maximum flux is far less than the saturation flux under DM as well as the integrated inductor of the IMSEF under CM. The power loss in the integrated inductors are mainly depended on the core loss, copper loss, and air-gap loss, as the current ripple at the switching frequency has been largely reduced by the harmonic filter and the core loss could be small; the size of the EMI filtering inductor is small enough that the copper loss and air-gap loss can be ignored.

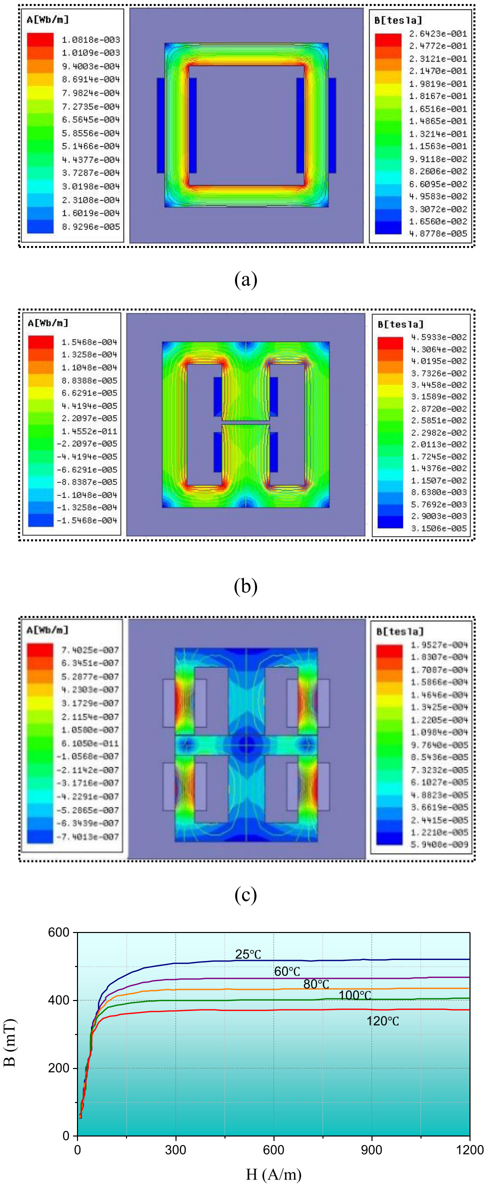

(a)

(b)

(c)

(d)

Fig. 15. Magnetic circuit analysis of the integrated inductor in the simulation. (a) Integrated inductor of the ISSEF under CM. (b) Integrated inductor of the ISSEF under DM. (c) Integrated inductor of the IMSEF under CM. (d) Saturation curve of the ferrite core under different temperatures [23].

In order to verify that the designed magnetic-integrated EMI filter will not adversely affect the output current of the inverter system, the influence of the EMI filter on the harmonic magnitude of the output current has been analyzed first. Harmonics is a relatively low-frequency form of DM noise, generally, depending on the characteristics of the EMI filter. It will not significantly affect the harmonics of the current, and only the DM part of the EMI filter will have a certain inhibitory effect on its output current harmonics. While compared to the harmonic filter, the DM part of the EMI filter generally has a quite smaller filter inductance and capacitance. Thus, under normal condition, its impact can be negligible.

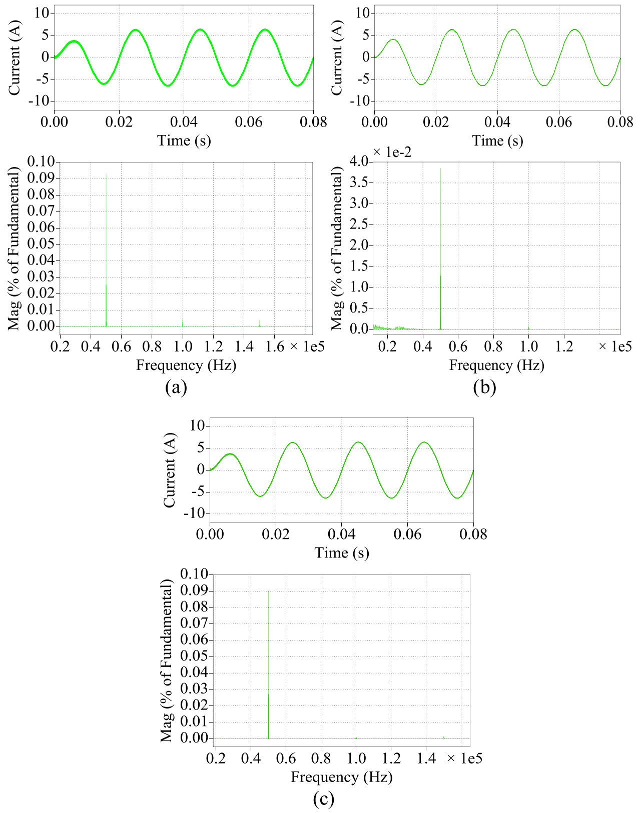

Fig. 16. Grid-side current waveforms and their THD analysis in simulation. (a) Without EMI filter, THD = 1.95%. (b) With ISSEF, THD = 1.84%. (c) With IMSEF, THD = 1.76%.

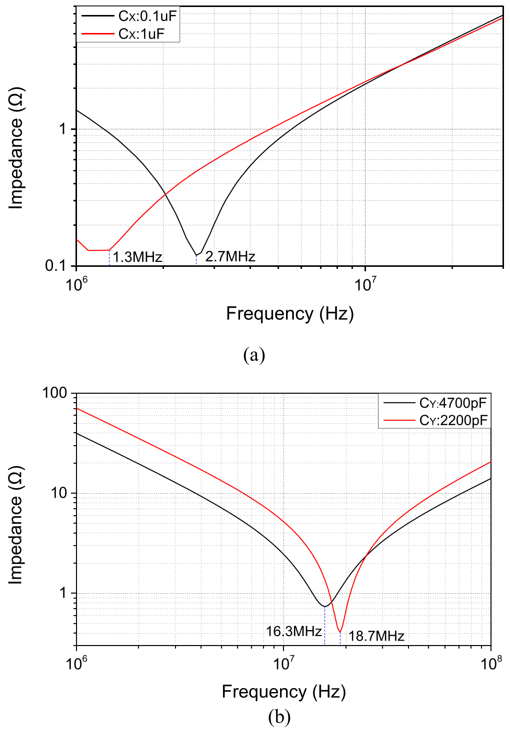

Fig. 17. Impedance measurement of the DM and CM capacitors. (a) DM capacitors. (b) CM capacitors.

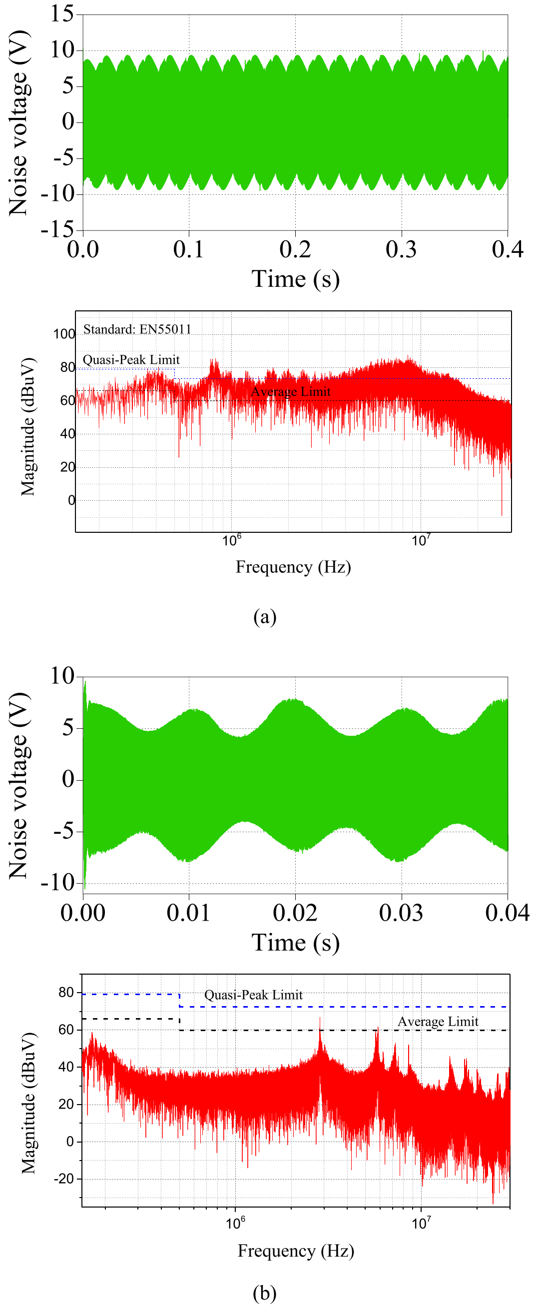

Fig. 18. Conducted EMI noise voltage and spectrum in the simulation. (a) Original EMI noise. (b) With the ISSEF.

Fig. 16 shows the grid-side current and their THD analysis with different types of EMI filters in the simulation. Overall, no significant influence has been observed by the ISSEF and IMSEF compared to the current harmonics without EMI filter, only a slightly smaller at low frequency band (<150 kHz). While according to the comparison between Figs. 16(b) and (c), it can be seen that IMSEF contains a slightly better harmonic attenuation ability when compared to ISSEF, showing that better DM suppression of IMSEF would be performed.

During the design procedure of the IMSEF, the DM capacitor is chosen as 1 μF instead of the 0.1 μF of the ISSEF to ensure

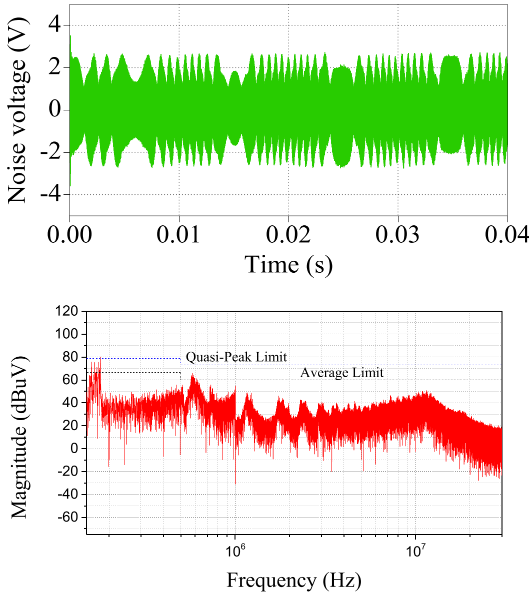

(a)

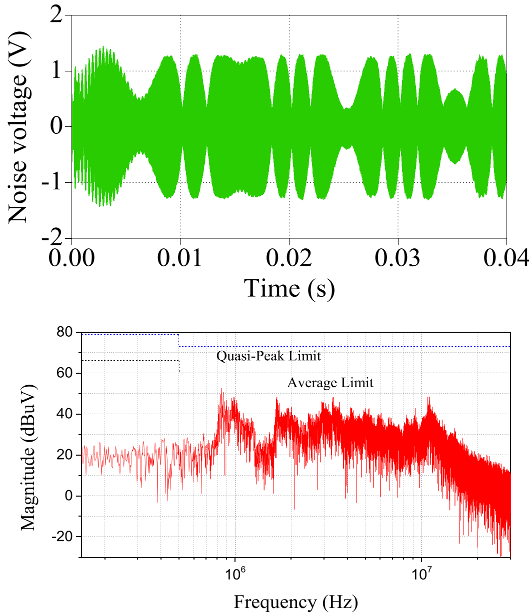

(b)

Fig. 19. Conducted EMI noise voltage and spectrum in the simulation. (a) With the IMSEF (C_Y: 2200 pF). (b) With the IMSEF (C_Y: 4700 pF).

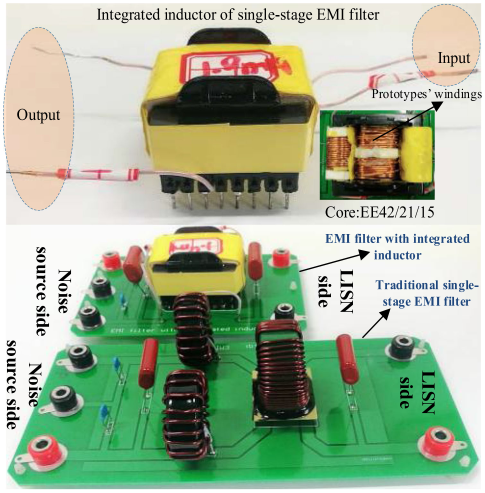

(a)

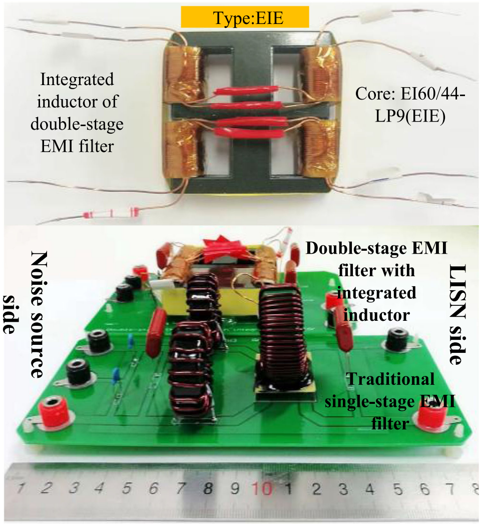

(b)

Fig. 20. Size comparison between the integrated EMI filter and a traditional discrete SSDEF. (a) ISSEF and a traditional discrete single-stage PEF. (b) IMSEF and a traditional discrete single-stage PEF.

TABLE III
SIZE AND WEIGHT COMPARISON

Parameters	SSDEF	ISSEF	IMSEF
Inductor volume (mm^3)	80525.3	24693.0	76800.0
Inductor weight (g)	243.1	136.8	300.9
PCB Area (mm^2)	15300	9600	15000
Filter Volume (mm^3)	612000	336000	375000

DM noise suppression ability. The impedance curves of the 0.1 μF and 1 μF capacitors are shown in Fig. 17(a). The 1 μF capacitor can provide a lower impedance below 2 MHz, especially in the range of 150 kHz–1 MHz, which can effectively bypass the EMI noise in this frequency range. The impedance curves of the CM capacitors are shown in Fig. 17(b), which show satisfactory capacitance characteristics, ensuring the high-frequency CM noise suppression ability.

The simulated conducted EMI results without EMI filter and with ISSEF are shown in Fig. 18. It can be found that the EMI noise is reduced by the ISSEF apparently. According to the comparison between Fig. 18 and 19, both the ISSEF and IMSEF have an effective EMI suppression ability. On the other hand, the CM inductor of the IMSEF (0.54 mH) is designed based on the originally selected CM capacitor (2200 pF), while the resonance frequency ($f_{r2} =$ 167.06 kHz) is larger than 150 kHz, and the magnitude is increased about 15 dB near 167 kHz as shown in Fig. 19(a). Without exceeding the leakage current standard [24], the CM capacitor is adjusted to be 4700 pF to ensure f_{r2} below 150 kHz. As can be seen in Fig. 19(b), the IMSEF shows slightly better performance than ISSEF, especially from 150 kHz to 1 MHz, the negative effect of the IMSEF can also be avoided

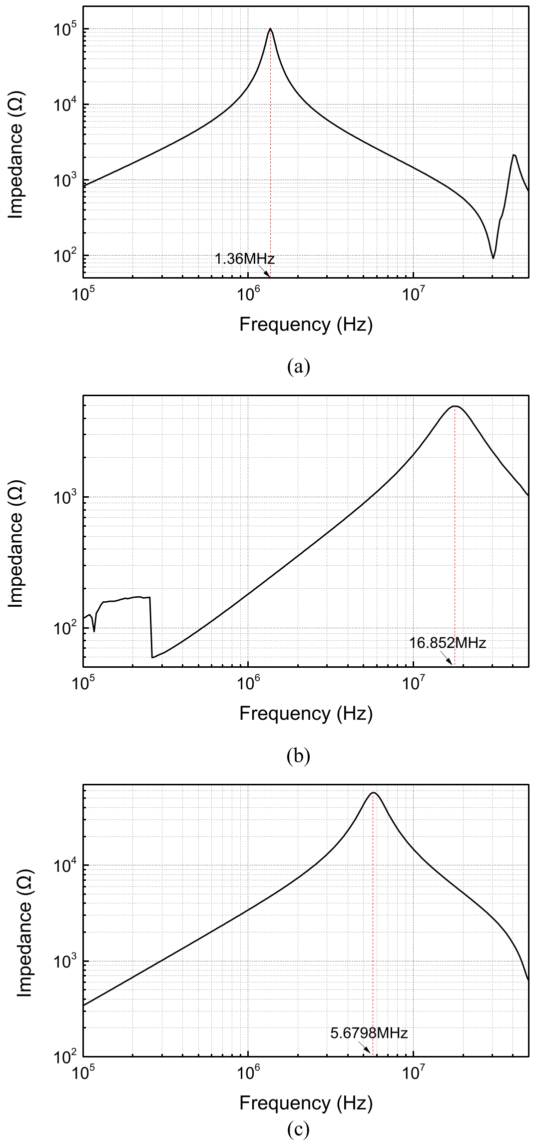

(a)

(b)

(c)

Fig. 21. High-frequency impedance of the integrated inductor. (a) CM inductor of ISSEF. (b) DM inductor of ISSEF. (c) CM inductor with IMSEF.

with the CM capacitor adjustment and the total EMI noise can be reduced in the range of 150 kHz to 30 MHz.

V. EXPERIMENT RESULTS

An experiment is conducted to verify the feasibility of the proposed magnetic integration methods of the PEF. A 500-W SiC single-phase VSI is applied in the experiment platform and the system parameters are consistent with the simulation. The designed integrated inductors, ISSEF and IMSEF, are shown in Fig. 20.

Size and weight comparison between the integrated EMI filter and a traditional single-stage discrete EMI filter (SSDEF) are shown in Table III. The total volumes of the ISSEF and IMSEF can be reduced by approximately 40% compared with the SSDEF; the PCB area has been reduced by 37.3% with ISSEF and 2% with IMSEF. The inductor volume has been reduced by 69% and 4.6% with ISSEF and IMSEF, respectively. There has been a 43.7% weight reduction with the integrated inductor in ISSEF, while the weight with the integrated inductor in IMSEF has 23.8% increment.

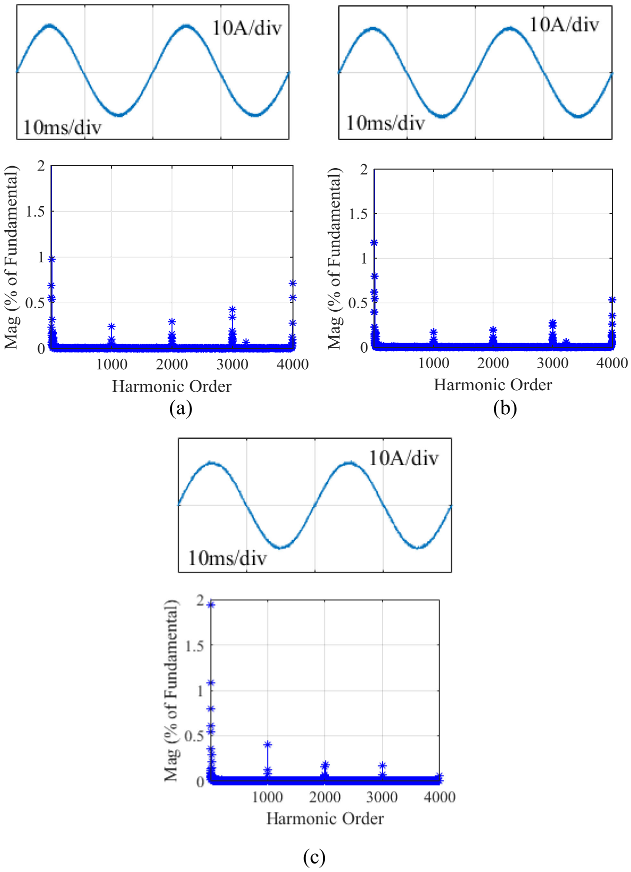

(a)

(b)

(c)

Fig. 22. Grid-side current waveforms and their THD analysis in the experiment. (a) Without EMI filter, THD = 3.08%. (b) With ISSEF, THD = 2.89%. (c) With IMSEF, THD = 2.64%.

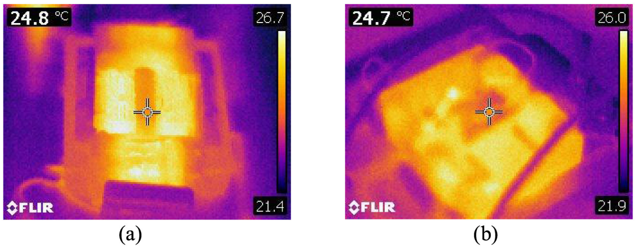

(a)

(b)

Fig. 23. Magnetic core temperature in experiments under full load. (a) ISSEF. (b) IMSEF.

Fig. 21 depicts the high-frequency performance of the integrated inductor of ISSEF and IMSEF measured with an impedance analyzer (HIOKI IM7581-01). The equivalent CM inductor of ISSEF is about 1.35 mH (around 4% error); the resonant frequency is 1.36 MHz. In the frequency range 150 kHz–10 MHz, the CM inductor can provide a satisfactory impedance for EMI reduction, but the attenuation would become relatively worse between 10–30 MHz. The equivalent DM inductor of ISSEF is about 29.3 μH (around 13.8% error). The DM inductance fully meets the requirement, and the resonant frequency is 16.852 MHz, which shows a

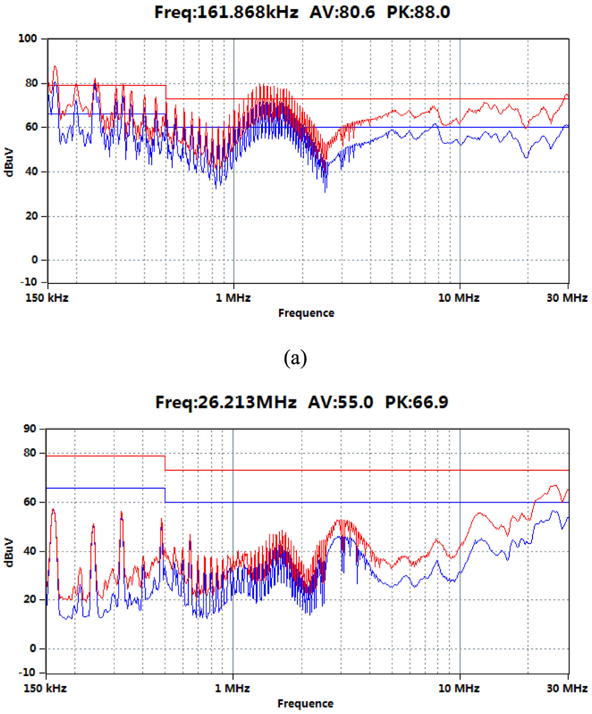

(a)

(b)

Fig. 24. CM EMI noise in the experiments. (a) Original CM EMI. (b) CM EMI with the SSDEF.

satisfied high-frequency attenuation performance. The equivalent CM inductance of IMSEF is about 561 μH (around 3.9% error) and the resonant frequency is 5.6798 MHz. It can provide a satisfactory impedance for the CM EMI reduction in 150 kHz–30 MHz.

On the other hand, in the experiments, the influence of different integrated EMI filters on the grid-side current harmonics has also been analyzed; Fig. 22 shows that the THD of the output current without EMI filter, with ISSEF and IMSEF are 3.08%, 2.89%, and 2.64%, respectively. It can be seen that the designed integrated inductors have no significant influence on the low-frequency harmonics. The DM inductance of ISSEF is small (nearly 26 μH) and the IMSEF is leakage inductance, thus, the relatively low-frequency harmonics would be restrained slightly. From the comparison between Fig. 22(b) and (c), the IMSEF shows a slightly better low-frequency harmonic suppression performance.

As most of the ripple current at switching frequency has been reduced by the harmonic filter, the core loss at the EMI filtering inductors would be very small, which can be ignored. Fig. 23 shows the steady-state temperature of the magnetic core measured by a thermal camera under full load at room temperature (20 °C). The temperature of both the ISSEF and IMSEF increase a bit, thus, the cores could maintain a high saturation flux according to the previous analysis in Section IV, which ensures the effective performance of the filtering inductors.

A (50 μH + 5 Ω)|| 50 Ω V-type LISN with a CM and DM noise separator is applied for the EMI measurements conducted in the experiments. The CM noise measurement without EMI filter is shown in Fig. 24(a). As can be seen from Fig. 24(b) and Fig. 25(a), the noise attenuation of ISSEF is basically consistent with SSDEF; only the low-frequency (500 kHz–4 MHz) attenuation is slightly worse in the SSDEF.

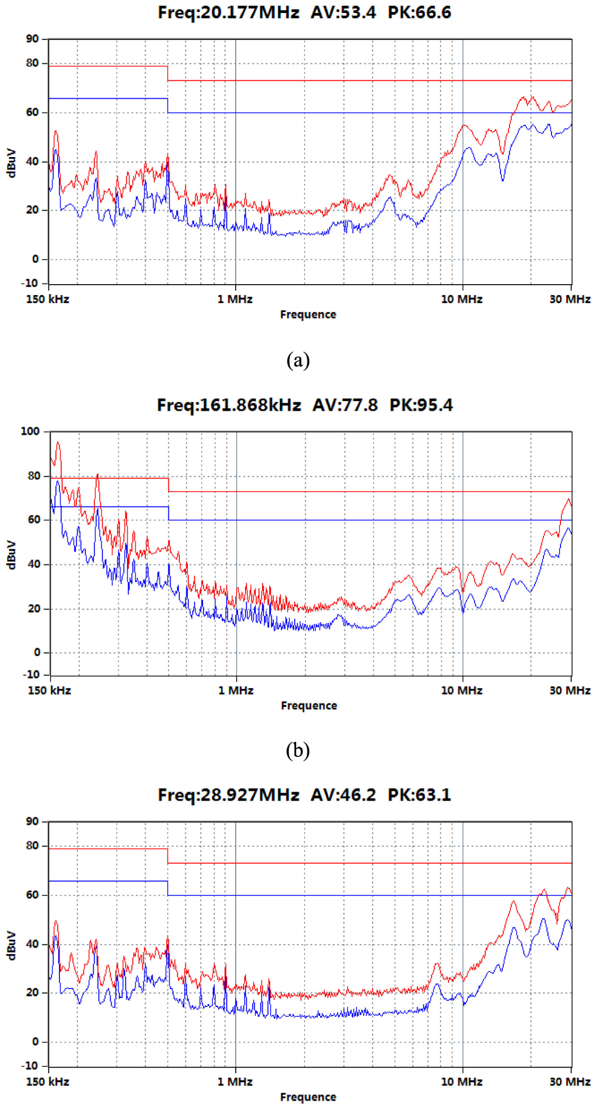

(a)

(b)

(c)

Fig. 25. CM EMI noise in the experiments. (a) CM EMI with the ISSEF. (b) CM EMI with the IMSEF (C_Y: 2200 pF). (c) CM EMI with the IMSEF (C_Y: 4700 pF).

According to the comparison among Fig. 25(a)–(c), both the ISSEF and IMSEF can reduce the CM EMI noise largely. The effectiveness of ISSEF in the frequency range of 10–20 MHz is slightly lower due to the better high-frequency impedance performance of CM inductors in IMSEF. In addition, the CM EMI suppression ability of the IMSEF with 2200 pF is shown for comparison. Instead, the CM EMI at approximately 161.868 kHz is increased by 10 dB, as shown in Fig. 25(b). According to (7), f_{r1} and f_{r2} of the equivalent CM EMI filter are 63.8 and 167.06 kHz, respectively. f_{r2} is larger than 150 kHz, that leads to an unsatisfactory attenuation result. However, this situation can be avoided by adjusting the CM capacitor to be

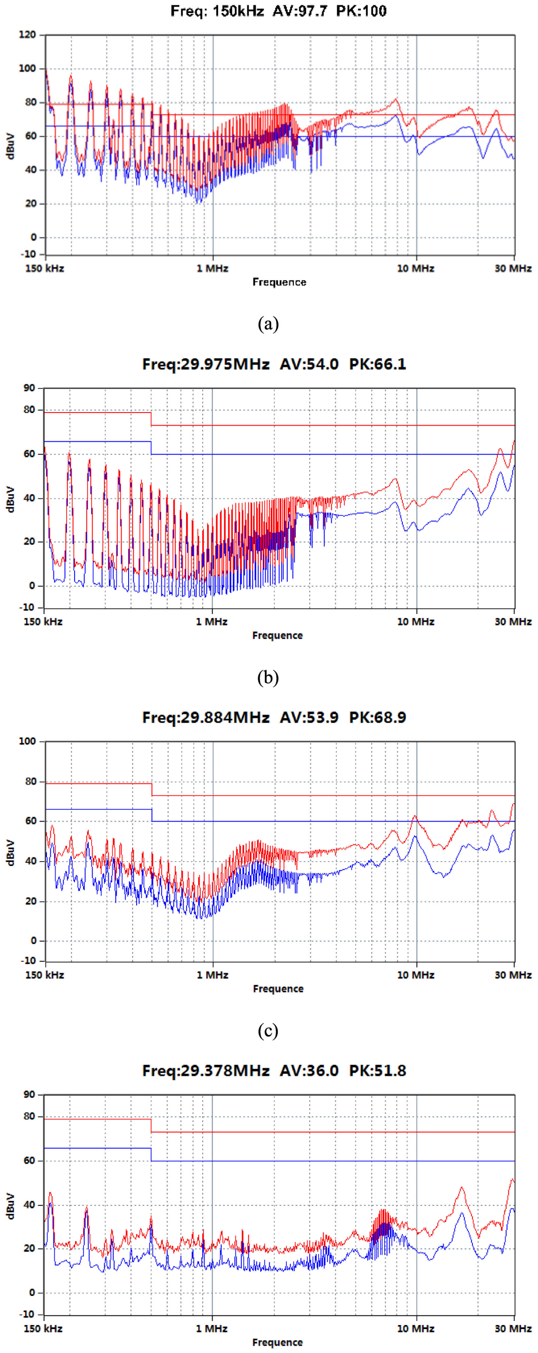

(a)

(b)

(c)

(d)

Fig. 26. DM EMI noise in the experiments. (a) Original DM EMI. (b) DM EMI with the SSDEF. (c) DM EMI with the ISSEF. (d) DM EMI with the IMSEF.

appropriately 4700 pF which is larger than the original 2200 pF. The resonant frequency points f_{r1} and f_{r2} are reduced to be 43.657 and 114.3 kHz, respectively, which are far less than 150 kHz. The suppressed EMI noise measurement is shown in Fig. 25(c), noise amplification situation is avoided and there is a large degree of attenuation at the relatively low frequency range.

Fig. 26(a) shows the DM EMI noise without EMI filter that the noise exceeds the EMI standard. Compared with Fig. 26(b)–(d), it can be found that both the ISSEF and IMSEF could reduce the EMI noise below the standard; the DM EMI noise can be reduced below the limit in the frequency range of 150 KHz–30MHz due to the satisfied high-frequency performance of the filtering components. The DM attenuation of ISSEF and SSDEF are highly consistent with each other from the comparison between Fig. 26(b) and (c), which shows the accuracy and effective design. According to the comparison between Fig. 26(c) and (d), it can be found that the DM noise has a higher attenuation with IMSEF, which shows the better EMI reduction ability of IMSEF.

VI. CONCLUSION

In this paper, the magnetic integration of single-stage and multi-stage EMI filters are designed, modeled, and analyzed. The magnetic circuit and EMI suppression ability have been analyzed in a simulation to verify the feasibility of the structure and parameters design. A 500-W SiC single-phase grid-connected VSI is built and applied in the experiment. The simulation and experimental results show satisfactory EMI suppression performance for the proposed ISSEF and IMSEF. On the other hand, according to the size and weight comparison with SSDEF, 40% of the total volume and 69% of the inductor volume have been reduced by the integration method in ISSEF. Although the weight of integrated inductor of IMSEF has a 23.8% increment, the IMSEF shows a better EMI suppression ability and 4.6% inductor volume reduction.

REFERENCES

[1] S. Bernet, “Recent developments of high power converters for industry and traction applications,” *IEEE Trans. Power Electron.*, vol. 15, no. 6, pp. 1102–1117, Nov. 2000.

[2] J. R. Rodriguez, J. W. Dixon, J. R. Espinoza, J. Pontt, and P. Lezana, “PWM regenerative rectifiers: State of the art,” *IEEE Trans. Ind. Electron.*, vol. 52, no. 1, pp. 5–22, Feb. 2005.

[3] M. H. Hedayati and V. John, “Novel integrated cm inductor for single-phase power converters with reduced EMI,” *IEEE Trans. Ind. Appl.*, vol. 53, no. 2, pp. 1300–1307, Mar./Apr. 2017.

[4] M. Hosseinipour, M. N. Soorki, and M. Ahmadian, “On effective electromagnetic shielding of modern pulsewidth modulating adjustable speed drives,” *IEEE Trans. Electromagn. Compat.*, vol. 60, no. 4, pp. 875–884, Aug. 2018.

[5] “Industrial, scientific and medical equipment—Radio-frequency disturbance characteristics—Limits and methods of measurement,” International Electrotechnical Commission, Geneva, Switzerland, 2016.

[6] G. Ala, G. C. Giaconia, G. Giglia, M. C. D. Piazza, and G. Vitale, “Design and performance evaluation of a high power-density EMI filter for PWM inverter-fed induction-motor drives,” *IEEE Trans. Ind. Appl.*, vol. 52, no. 3, pp. 2397–2404, May/Jun. 2016.

[7] D. Hamza, M. Qiu, and P. K. Jain, “Application and stability analysis of a novel digital active EMI filter used in a grid-tied PV microinverter module,” *IEEE Trans. Power Electron.*, vol. 28, no. 6, pp. 2867–2874, Jun. 2013.

[8] W. Chen, X. Yang, and Z. Wang, “An active EMI filtering technique for improving passive filter low-frequency performance,” *IEEE Trans. Electromagn. Compat.*, vol. 48, no. 1, pp. 172–177, Feb. 2006.

[9] D. Shin *et al.*, “Analysis and design guide of active EMI filter in a compact package for reduction of common-mode conducted emissions,” *IEEE Trans. Electromagn. Compat.*, vol. 57, no. 4, pp. 660–671, Aug. 2015.

[10] X. Wu, D. Xu, Z. Wen, Y. Okuma, and K. Mino, “Design, modeling, and improvement of integrated EMI filter with flexible multilayer foils,” *IEEE Trans. Power Electron.*, vol. 26, no. 5, pp. 1344–1354, May 2011.

[11] R. Lai, Y. Maillet, F. Wang, S. Wang, R. Burgos, and D. Boroyevich, "An integrated EMI choke for differential-mode and common-mode noise suppression," *IEEE Trans. Power Electron.*, vol. 25, no. 3, pp. 539–544, Mar. 2010.

[12] M. H. Hedayati and V. John, "A novel integrated CM inductor for parallel converters with interleaved carrier," in *Proc. IEEE Int. Conf. Power Electron., Drives Energy Syst.*, 2014, pp. 4–6.

[13] H. Huang, L. Deng, B. Hu, and G. Wei, "Techniques for improving the high-frequency performance of the planar CM EMI filter," *IEEE Trans. Electromagn. Compat.*, vol. 55, no. 5, pp. 901–908, Oct. 2013.

[14] R. Chen, J. D. V. Wyk, S. Wang, and W. G. Odendaal, "Improving the characteristics of integrated EMI filters by embedded conductive layers," *IEEE Trans. Power Electron.*, vol. 20, no. 3, pp. 611–619, May 2005.

[15] R. Chen, J. Van Wyk, S. Wang, and W. Odendaal, "Planar electromagnetic integration technologies for integrated EMI filters," in *Proc. 38th IAS Annu. Meeting Conf. Rec. Ind. Appl. Conf.*, 2003, pp. 1582–1588.

[16] J. Fang, H. Li, and Y. Tang, "A magnetic integrated *LLCL* filter for grid-connected voltage-source converters," *IEEE Trans. Power Electron.*, vol. 32, no. 3, pp. 1725–1730, Mar. 2017.

[17] D. Pan, R. Xinbo, X. Wang, C. Bao, and L. I. Weiwei, "Magnetic Integration of the *LCL* filter in grid-connected inverters," *IEEE Trans. Power Electron.*, vol. 29, no. 4, pp. 1573–1578, Apr. 2014.

[18] Y. Liu, K. Y. See, K. J. Tseng, R. Simanjorang, and J. S. Lai, "Magnetic integration of three-phase *LCL* filter with delta-yoke composite core," *IEEE Trans. Power Electron.*, vol. 32, no. 5, pp. 3835–3843, May 2017.

[19] "Industrial, scientific and medical (ISM) radio-frequency equipment—Electromagnetic disturbance characteristics—Limits and methods of measurement," EN 55011 CISPR 11, 2009.

[20] "Designing complex magnetic components," 2019. [Online]. Available: https://www.plexim.com/plecs/magnetic

[21] W. G. Hurley and W. H. Wölfle, *Transformers and Inductors for Power Electronics: Theory, Design and Applications*. Hoboken, NJ, USA: Wiley, 2013.

[22] W. G. Hurley, T. Merkin, and M. Duffy, "The performance factor for magnetic materials revisited: The effect of core losses on the selection of core size in transformers," *IEEE Power Electron. Mag.*, vol. 5, no. 3, pp. 26–34, Sep. 2018.

[23] Nanjing New Conda Magnetic Industrial Co. Ltd. [Online]. Available: http://www.ncd.com.cn/down.asp?cid=195

[24] B. Yang, W. Li, Y. Gu, W. Cui, and X. He, "Improved transformerless inverter with common-mode leakage current elimination for a photovoltaic grid-connected power system," *IEEE Trans. Power Electron.*, vol. 27, no. 2, pp. 752–762, Feb. 2012.

Yitao Liu (S'11–M'15) received the B.S. degree in electrical engineering from Wuhan University, Wuhan, China, in 2008, and the M.S. and Ph.D. degrees in electrical and electronic engineering from Nanyang Technological University (NTU), Singapore, in 2009 and 2014, respectively.

From 2014 to 2015, he was a Research Fellow with the Rolls Royce-NTU Joint Laboratory. He is currently an Assistant Professor with the College of Mechatronics and Control Engineering, Shenzhen University, Shenzhen, China. His current research interests include high power density converters, EMI/EMC in power electronics, and wideband-gap devices.

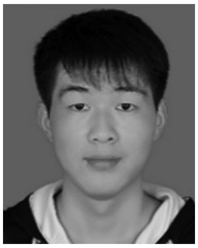

Shiqi Jiang received the B. Eng. degree in automation engineering from Hubei University of Technology, Wuhan, China, in 2017. He is currently working toward the M.Eng. degree at the College of Mechatronics and Control Engineering, Shenzhen University, Shenzhen, China. His research interests include EMI/EMC in the grid-connected inverters.

Weihua Liang received the B.Sc. degree in electrical engineering from Taiyuan Institute of Technology, Taiyuan, Shanxi, China, in 2012, and the Ph.D. degree in electrical engineering from Beijing Jiaotong University, Beijing, China, in 2018.

He is currently a Postdoctoral Fellow with Shenzhen University, Shenzhen, China. His research interests include electrical machine and drive, renewable energy generation, Z-source converters/inverters, etc.

Huaizhi Wang (M'16) received the B. Eng. and M. Eng. degrees in control science and engineering from Shenzhen University, Shenzhen, China, in 2009 and 2012, respectively, and the Ph.D. degree in electrical engineering from South China University of Technology, Guangzhou, China, in 2015.

From May 2014 to May 2015, he was a Research Assistant with the Department of Electrical Engineering, Hong Kong Polytechnic University, Hong Kong. In 2015, he joined the College of Mechatronics and Control Engineering in Shenzhen University as an Assistant Professor and was subsequently promoted to an Associate Research Professor in 2017. His research mainly focuses on cyber-attack, smart grid state estimation, and cyber physical power system.

Jianchun Peng (M'04–SM'17) received the B.S. and M.S. degrees in electrical engineering from Chongqing University, Chongqing, China, in 1986 and 1989, respectively. He received the Ph.D. degree in electrical engineering from Hunan University, Hunan, China, in 1981.

From November 2002 to November 2003, he was a Visiting Professor with Arizona State University, Tempe, AZ, USA, and from May 2006 to August 2006, with Brunel University, London, U.K. He is currently a Professor with the College of Mechatronics and Control Engineering, Shenzhen University, Shenzhen, China. His current research interests include electricity markets, and power system optimal operation and control.